Research Square

Preprints are preliminary reports that have not undergone peer review.
They should not be considered conclusive, used to inform clinical practice,
or referenced by the media as validated information.

$p\bar{p}$ production from QED vacuum excitation in high-energy nuclear collisions

Xin Wu

wuxinust@ustc.edu.cn

University of Science and Technology of China

Physical Sciences - Article

Keywords:

Posted Date: May 6th, 2026

DOI: https://doi.org/10.21203/rs.3.rs-9575649/v1

License: This work is licensed under a Creative Commons Attribution 4.0 International License.
Read Full License

Additional Declarations: There is **NO** Competing Interest.

$p\bar{p}$ production from QED vacuum excitation in high-energy nuclear collisions

The STAR Collaboration

April 30, 2026

Abstract

In Quantum Electrodynamics (QED), the vacuum is permeated by continuous quantum energy fluctuations, driven by zero-point motion resulting from the Heisenberg uncertainty principle, which briefly give rise to virtual particle-antiparticle pairs. Although these pairs normally annihilate almost instantaneously, sufficiently strong electromagnetic fields can force the charged particles apart and supply the energy needed to convert them into real, observable particles, i.e., the Schwinger mechanism. Relativistic heavy-ion collisions produce the most intense electromagnetic fields ever achieved in a laboratory, providing a unique setting to stimulate the QED vacuum and transform these fleeting fluctuations into tangible matter.

Here, we present the first observation of proton-antiproton ($p\bar{p}$) pairs produced at very low transverse momentum (p_T) in ultra-peripheral Au+Au collisions. A total of 96 $p\bar{p}$ candidates were identified in events with exactly 2 charged particle tracks, yielding a production cross section of $\sigma_{p\bar{p}} = 1.56 \pm 0.22\,(\text{stat.}) \pm 0.23\,(\text{syst.})$ μb. The measured yield exceeds estimated photonuclear backgrounds by about three orders of magnitude, supporting a predominantly two-photon origin. The observed $p\bar{p}$ pairs are compatible with QED vacuum excitation, where ultra-strong fields promote vacuum fluctuations into a six-quark system via a Schwinger-like mechanism which subsequently hadronizes into $p\bar{p}$. These findings deepen our understanding of QED vacuum properties under extreme electromagnetic fields and establish a new methodology for exploring more diverse vacuum decay channels beyond conventional Schwinger pair production through relativistic heavy-ion collisions.

1 Introduction

The concept of the vacuum—once thought of as a simple, empty space devoid of matter—has undergone a radical transformation with the advent of quantum theory [1–9]. In classical physics, the vacuum was considered an inert backdrop for material interactions. However, this notion was upended by quantum mechanics, which revealed the vacuum to be a dynamic, fluctuating arena [10]. At its core,

the vacuum is filled with transient particle-antiparticle pairs, constantly created and annihilated in accordance with the Heisenberg uncertainty principle [11, 12]. These quantum fluctuations, while imperceptible in daily life, leave their imprint through subtle yet measurable effects.

Experimental evidence for these quantum fluctuations first emerged through precision spectroscopy. In the 1930s, measurements of the hydrogen Hα line by Yu-Ming Xie and William V. Houston [13] revealed small discrepancies with the predictions of Dirac's relativistic quantum theory. Although not understood at the time, these anomalies foreshadowed what was definitively identified in 1947 as the Lamb shift [14]. Hans Bethe's [15] explanation of this anomaly through vacuum polarization effects solidified the quantum vacuum as a cornerstone of Quantum Electrodynamics (QED). The Casimir effect [16, 17] further validated QED, demonstrating that "empty" space is teeming with virtual photons. These insights raised a profound question: can these quantum fluctuations be converted into stable matter under extreme conditions such as those present during the early universe?

A striking theoretical answer was provided by Julian Schwinger in 1951 [18], who showed that an electric field exceeding a critical strength—now known as the Schwinger limit ($E_{\rm cr} \sim 10^{18}$ V/m)—would destabilize the vacuum and lead to the spontaneous production of electron-positron (e^+e^-) pairs. This mechanism offers a direct link between quantum field theory and macroscopic electromagnetic fields. However, despite its fundamental significance, experimental access to this regime remains challenging. Typically, strong laser fields are currently employed to explore these extreme electromagnetic conditions. However, despite remarkable advances in laser technology [19, 20], current or planned laser systems still fall short of achieving the Schwinger intensity limit by six orders of magnitude [21].

Relativistic heavy-ion collisions provide a novel method to address this question. At facilities like the Relativistic Heavy Ion Collider (RHIC) [22] and the Large Hadron Collider (LHC) [23], nuclei accelerated to near-light speeds generate electromagnetic fields with intensities far surpassing the Schwinger limit—exceeding 10^{23} V/m [1]. In ultra-peripheral collisions (UPCs), where the nuclei pass each other without nuclear overlap, the primary interaction arises from the coherent electromagnetic fields of the highly Lorentz-contracted ions [25–27]. These fields create dense fluxes of quasi-real photons [28–30], enabling photon–photon interactions that can produce particle–antiparticle pairs [31]. In this sense, UPC pair production offers an experimentally accessible realization of vacuum excitation in extreme electromagnetic fields, closely connected to the Schwinger mechanism introduced above.

In 2021, the Solenoidal Tracker at RHIC (STAR) collaboration [32, 33] made the first observation of e^+e^- pairs in Au+Au UPCs [34]. This marked a significant milestone, where the measured azimuthal angular modulation confirmed the suppression of the zero helicity state, providing direct experimental

[1] Estimating with $B = \frac{\mu_0}{4\pi}\frac{Ze\gamma\beta c}{x^2}$ for $x = 10$ fm (approximately twice the gold nuclear radius), the magnetic field at RHIC energy reaches $\sim 10^{15}$ T, corresponding to an electric field $E = cB > 10^{23}$ V/m. For comparison, the neutron star with the strongest magnetic field-a magnetar-has a magnetic field of $10^{10} - 10^{11}$ T [24].

evidence of the Breit-Wheeler process: the production of lepton pairs upon the collision of two real photons—the most fundamental mechanism of QED vacuum excitation [35]. In addition, ATLAS utilized the data from $\sqrt{s_{\rm NN}}$ =5.02 TeV Pb+Pb UPCs to experimentally observe the photon-photon elastic scattering process for the first time [36, 37]. These measurements provide compelling experimental evidence for probing quantum vacuum structure and light-to-matter conversion dynamics. Extending this paradigm from elementary lepton pairs to composite hadron–antihadron systems is, however, substantially more challenging. For the $\pi^+\pi^-$ photoproduction channel, the main contribution comes from the decay of the ρ^0 resonance. Moving to the K^+K^- channel, the ALICE collaboration took an important step by measuring its photoproduction [38]; however, limited statistics and substantial photonuclear (γA) contributions restricted its sensitivity to a clean two-photon ($\gamma\gamma$) component.

Now, studying the photoproduction of proton-antiproton pairs in UPCs offers a new opportunity to address this question. Protons, the simplest and the most abundant atomic nuclei in the observable universe, are composite particles governed by Quantum Chromodynamics (QCD). The process $\gamma\gamma \to p\bar{p}$ (Fig. 1a) entails extracting three quarks and three antiquarks from the vacuum and assembling them into stable hadrons. Sitting at the intersection of strong-field QED and non-perturbative QCD, this process poses considerable theoretical challenges that have so far hindered predictions. Since the 1980s, a series of related studies have been conducted in electron-positron collider experiments [39–44]. Taken together, these e^+e^- measurements cover diverse tagging strategies and kinematics, making direct comparisons nontrivial and a unified description in the few-GeV region challenging because hard and non-perturbative dynamics are intertwined. Relativistic heavy-ion UPCs offer a complementary environment to revisit this process under markedly different electromagnetic-field conditions. In UPCs, coherent photon emission from relativistic nuclei leads to quasi-real photons whose virtuality is controlled primarily by the nuclear size and form factor, and is typically one to two orders of magnitude lower than in e^+e^- collisions [45]. Moreover, the associated electromagnetic fields are extremely intense and slowly varying on the relevant scales, bringing the system closer to the classical-field conditions underlying Schwinger-like vacuum excitation—namely, the conversion of vacuum fluctuations into real particle pairs.

In this work, we report the first observation of proton-antiproton pair production via QED-driven vacuum excitation. Our analysis is based on data from Au+Au UPCs at collision energies of $\sqrt{s_{\rm NN}} = 200$ GeV-corresponding to gold ions accelerated to 99.996% of the speed of light-with the STAR experiment at RHIC. Analyzing 1.06×10^8 UPC events, we identified 96 $p\bar{p}$ candidates with transverse momenta $p_T^{p\bar{p}} < 100$ MeV/c, a hallmark of photon-photon collisions. The measured cross-section, $\sigma_{p\bar{p}} = 1.56 \pm 0.22\,(\text{stat.}) \pm 0.23\,(\text{syst.})$ μb, exceeds expectations from photonuclear backgrounds by three orders of magnitude [46], conclusively establishing a two-photon origin.

This discovery extends vacuum excitation phenomena beyond lepton production to baryon production, demonstrating that vacuum excitation can coherently materialize multi-quark systems. It challenges theorists to develop coupled

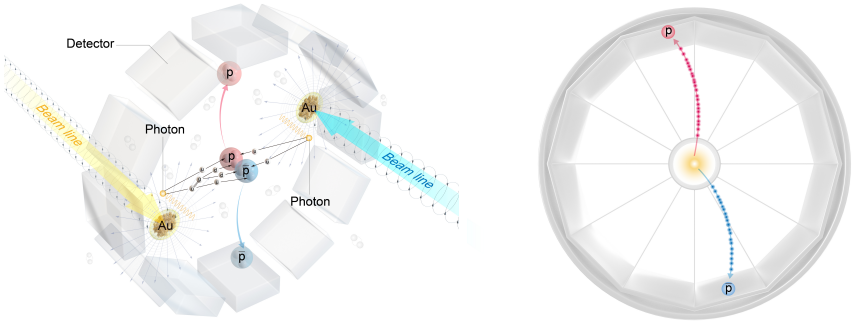

(a) (b)

Figure 1: (a)Fast-moving gold nuclei carry extremely strong electromagnetic fields. The proton-antiproton pairs generated from vacuum quantum fluctuation are separated by the electromagnetic fields and travel to the detectors. (b) Sectional-view projection of the geometry illustrated in panel (a) for a photoproduced $p\bar{p}$ event in an Au+Au UPC. The particles ionize the Time Projection Chamber gas, and their resulting three-dimensional trajectories, curved by the magnetic field, are projected onto this two-dimensional plane.

QED-QCD descriptions for extreme electromagnetic environments. Furthermore, our results validate relativistic heavy-ion collisions as a unique tool for exploring vacuum decay modes at field strengths ($\sim 10^{23}$ V/m) that are currently inaccessible to laser-based experiments.

2 Proton-antiproton candidate selection

This analysis uses data collected from the STAR detector at RHIC. The STAR detector combines a suite of specialized detectors [33] with a high-performance data acquisition system (DAQ) [47]. This configuration, originally designed for quark-gluon plasma (QGP) studies [48], has proven effective for investigating electromagnetic interactions in UPCs. Among the numerous sub-detector systems, the Zero Degree Calorimeter [49] (ZDC), Beam-Beam Counter [50] (BBC), and Time of Flight [51] (TOF) detector provided the essential triggers for UPC event selection in this analysis. These detectors exploited the distinct signatures of UPC events-particularly their low number of produced particles and absence of combinatorial background-to efficiently isolate them from typical hadronic interactions (Details are provided in Method A.1).

The Time Projection Chamber (TPC) [52], serving as the centerpiece of the STAR detector, supplied the critical information for particle reconstruction and identification (Details are provided in Method A.2) [53, 54]. The unique energy loss of different particles provides essential information for particle identification. For each individual trajectory (or "track"), the average energy loss $\langle dE/dx \rangle_{\rm track}$

is calculated from all its reconstructed space points along the trajectory in the TPC. The deviation of this measured $\langle dE/dx \rangle_{\text{track}}^{\text{Measured}}$ from its theoretical expectation $\langle dE/dx \rangle_{\text{track}}^{\text{Theory}}$ for a particle species X, normalized by the detector resolution R, is expressed as $n\sigma_X$:

$$n\sigma_X = \frac{1}{R} \log \frac{\langle dE/dx \rangle_{\text{track}}^{\text{Measured}}}{\langle dE/dx \rangle_{\text{track}}^{\text{Theory}}}. \tag{1}$$

Here, the resolution R is defined as the standard deviation of the $\langle dE/dx \rangle_{\text{track}}$ distribution divided by its mean value, obtained from a sample of minimum ionizing particles.

This analysis is based on approximately 1.06×10^8 UPC events from Au+Au collisions at $\sqrt{s_{\text{NN}}} = 200$ GeV collected in 2010, 2011 and 2014. Since our primary focus is the process $\gamma\gamma \to p\bar{p}$, we require each event to contain exactly two charged particles originating directly from the collision vertex (Fig. 1b). Such trigger-level and event-level cuts filter out over 99.9% of the hadronic interaction background [55]. To select proton-antiproton ($p\bar{p}$) pairs with high purity, we apply, in addition, the criterion $\chi^2_{p\bar{p}} < 4$, $n\sigma_e > 2$ and $n\sigma_\pi > 3$ (Details are provided in Method A.2 and A.5), where $\chi^2_{p\bar{p}}$ is defined as:

$$\chi^2_{p\bar{p}} = n\sigma_p^2 + n\sigma_{\bar{p}}^2. \tag{2}$$

For the coherent photoproduction process, each photon couples to its entire nucleus; thus, the transverse momentum of the equivalent photon ($p_{\text{T}}^{\text{photon}}$) is approximately inversely proportional to R_{nucleus}, as expected from the uncertainty principle[2], resulting in a value on the order of 0.1 GeV/c. Consequently, the products of this process also exhibit transverse momenta of this order, which is distinctly lower than those originating from strong interaction processes. Hence, we select the transverse momentum range of 0 to 0.2 GeV/c for our analysis. Concurrently, to suppress the background from vector meson decays originating from photonuclear interactions and to account for detector efficiency effects, the invariant mass window of 2.05 to 2.4 GeV/c^2 and the $p\bar{p}$ pair rapidity $|Y^{p\bar{p}}| < 0.5$ are adopted. After applying the $p\bar{p}$ pair rapidity requirements ($|Y^{p\bar{p}}| > 0.05$) to reject cosmic rays (Details are provided in Method A.3), a total of 96 $p\bar{p}$ pairs were identified in the mass and p_T region of interest (Details are provided in Method A.4). This marks the first observation of $p\bar{p}$ pairs produced in UPCs.

3 $p\bar{p}$ cross section

The differential cross sections $\frac{d\sigma}{dM}$ and $\frac{d\sigma}{dp_T}$ were extracted on a year-by-year basis to account for variations in detector efficiency over different data-taking periods:

$$\frac{d\sigma}{dM} = \frac{N(\Delta M)}{\Delta M \times \epsilon \times L} \qquad \frac{d\sigma}{dp_T} = \frac{N(\Delta p_T)}{\Delta p_T \times \epsilon \times L}, \tag{3}$$

[2]The transverse momentum of the equivalent photon can be estimated using the uncertainty principle: $\Delta x \cdot \Delta p \simeq \hbar c \Rightarrow R_{\text{nucleus}} \cdot p_T^{\text{photon}} \simeq \hbar c \Rightarrow p_T^{\text{photon}} \simeq \hbar c / R_{\text{nucleus}}$.

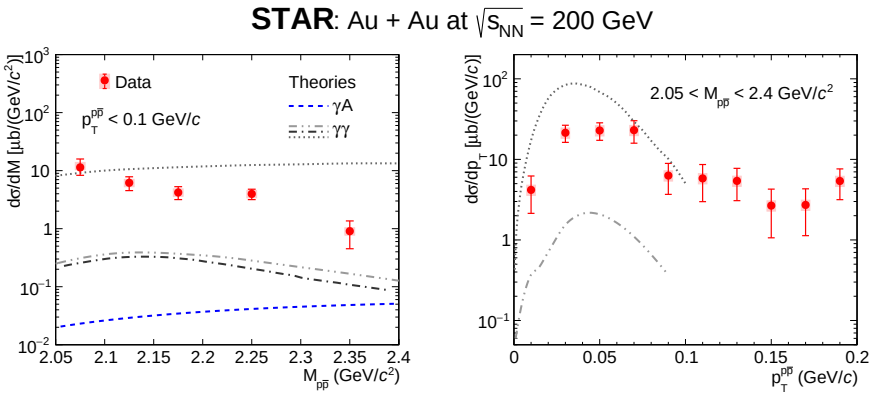

Figure 2: The invariant mass spectrum for $p_T^{p\bar{p}} < 0.1$ GeV (left panel) and the p_T spectrum for $2.05 < M_{p\bar{p}} < 2.4$ GeV/c^2(right panel) within the acceptance: $0.05 < |Y^{p\bar{p}}| < 0.5, p_T^{p(\bar{p})} > 0.2$ GeV/c, $|\eta^{p(\bar{p})}| < 0.9$, compared with theoretical calculations. The dashed curve [56] represents the theoretical calculation for the γA process. The dotted curve, dash-dotted curve and dash-double-dotted curve [57, 58] represent the theoretical calculation for the $\gamma\gamma$ process.

where N is the number of counts in different intervals of M or p_T, ΔM and Δp_T are the corresponding ranges, ϵ is the detector efficiency, and L is the luminosity (Details are provided in Method A.6 and A.7). Details of the systematic uncertainties can be found in Method A.8. To obtain a combined measurement, the cross sections from individual years were weighted according to their respective statistical uncertainties (Details are provided in Method A.9). Figure 2 presents the differential cross section as a function of the invariant mass (left panel) of the $p\bar{p}$ pairs, corresponding to the total energy of the $p\bar{p}$ system in its center-of-mass frame, and the p_T (right panel) of the $p\bar{p}$ pairs. The $\frac{d\sigma}{dM}$ exhibits continuity across the measured invariant mass range and the $\frac{d\sigma}{dp_T}$ is primarily concentrated in the region where $p_T < 0.1$ GeV/c. These observations strongly indicate that the $p\bar{p}$ pairs are predominantly produced through photon-induced processes.

Accurate background estimation is crucial for deriving robust physical conclusions. In this study, the physical background refers to processes other than the production of $p\bar{p}$ pairs with extremely low transverse momentum arising from QED vacuum excitation. Such backgrounds primarily originate from photonuclear interactions (the contribution of pomeron-pomeron fusion is strongly suppressed due to the UPC conditions that minimize hadronic overlap), which exhibit kinematic characteristics indistinguishable from QED vacuum excitation, precluding their removal via selection requirements. The estimation of these backgrounds is therefore based on theoretical calculations.

Photonuclear interactions can be categorized into resonant and non-resonant production. Resonant production occurs when equivalent photons emitted by one nucleus scatter off one another, producing a vector meson ($J^P = 1^-$)

due to spin conservation. This mechanism has been extensively studied both experimentally [59–63] and theoretically [64–66]. In this analysis, all vector mesons that decay to $p\bar{p}$ or $p\bar{p}+X$ (where X represents any additional particle) were considered. Following the Particle Data Group (PDG) manual [67], the relevant vector mesons include J/ψ, $\chi_{c0}(1P)$, $\chi_{c2}(1P)$, $\psi(2S)$, and $\psi(3770)$. Given their narrow widths and the challenges associated with producing heavier vector mesons via photonuclear interactions, the analysis focuses on the J/ψ state, whose mass lies closest to the measurement region.

Theoretical calculations, based on the Vector Meson Dominance (VMD) model [56] coupled with the Glauber approach [68], predict a cross section of approximately $10^{-7}\mu b$ for the process $Au+Au \to Au+Au+J/\psi$ within the measured region, which is negligible for this study. For the $p\bar{p}+X$ channel, the back-to-back production of $p\bar{p}$ and X in the vector meson's rest frame results in $p\bar{p}$ pairs with relatively large transverse momentum relative to the typical transverse momentum of photoproduction, thereby excluding their contribution to the measured region. Non-resonant production involves a virtual photon fluctuating into a virtual $p(\bar{p})$ and a real $\bar{p}(p)$ [69, 70]. Recent measurements by the GlueX collaboration of the scattering cross section for $\gamma p \to p\bar{p}+p$ [71] provide experimental constraints for estimating the non-resonant $p\bar{p}$ photoproduction cross section in relativistic heavy-ion collisions. The calculated photonuclear contribution is three orders of magnitude lower than the measured cross section, as shown in Fig. 2 dashed curve. These theoretical estimates strongly support the conclusion that the observed $p\bar{p}$ pairs predominantly arise from photon-photon interaction.

Moreover, our experimental results are compared in detail with predictions from two theoretical models for photon-photon interactions [57, 58] (dotted curve and dash-double-dotted curve in Fig. 2). The dotted curve considers the contribution from the dominant t-channel and describes the proton charge distribution using the Woods-Saxon form. The dash-double-dotted curve additionally includes contributions from the s-channel and the handbag diagram, and data from the process $\gamma\gamma \to p\bar{p}$ in e^+e^- collisions was used to constrain some parameters in the vertex function. This process, which produces proton-antiproton pairs, inherently involves an interplay between QED and non-perturbative QCD, posing significant challenges to theoretical calculations. Predictions from different models vary considerably, underscoring the current uncertainties in theoretical descriptions of such processes.

We also compared our results with the cross sections measured in electron-positron collider experiments [72]. The cross section of $\gamma\gamma \to p\bar{p}$ was determined by measuring the reaction $e^+e^- \to e^+e^-p\bar{p}$ and normalizing it with the two-photon luminosity $\frac{d^2N_{\gamma\gamma}}{dMdY}$ generated by the electron and positron beams, where M and Y represent the invariant mass and rapidity of the $p\bar{p}$ pair, respectively. To enable a direct comparison between our results and the measurements obtained from electron-positron collision experiments, we multiplied BELLE's measured cross section, $\sigma(\gamma_1\gamma_2 \to p\bar{p})$, by the two-photon luminosity, $\frac{d^2N_{\gamma\gamma}^{AuAu}}{dMdY}$ induced in Au+Au collisions [73, 74]. This allowed us to derive the cross section for

$Au + Au \to Au + Au + p\bar{p}$ as follows:

$$\sigma_{AuAu\to AuAup\bar{p}} = \int\int \frac{d^2N^{AuAu}_{\gamma\gamma}}{dMdY}\sigma(\gamma_1\gamma_2 \to p\bar{p})dY\,dM. \tag{4}$$

The calculated cross section is shown as the dash-dotted curve in Fig. 2. Interestingly, BELLE's measured cross sections are one to two orders of magnitude smaller than the results obtained in this study. A key distinction between the two environments is the typical photon virtuality: in e^+e^- collisions the two-photon process samples a broader spectrum of virtualities ($\sim 10^{-2}$ GeV^2) due to the sizeable deflections of the radiating leptons, whereas in UPCs the coherent photon emission is constrained by the nuclear form factor and is therefore much closer to the quasi-real limit ($\sim 10^{-3}$ GeV^2) [75]. For elementary final states such as dilepton production, once the appropriate photon fluxes are accounted for, measurements in e^+e^- collisions and UPCs are mutually consistent, as expected for a point-like process governed by perturbative QED. For composite hadrons, however, $\gamma\gamma \to p\bar{p}$ entails multi-quark production followed by confinement and hadronization, and the mapping from e^+e^- to heavy ions via a simple two-photon flux rescaling (often heuristically associated with a Z^4 enhancement) may no longer be sufficient. In this regime, non-perturbative QCD dynamics—such as quark–gluon dressing, hadronization, and possible coherence effects—could be amplified in the ultra-strong, quasi-classical fields of relativistic heavy ions, enhancing baryon–antibaryon yields relative to expectations anchored to e^+e^- data. If confirmed, such an environment-dependent modification would provide new empirical constraints on $\gamma\gamma \to$ hadrons in a regime directly relevant to hadronic light-by-light (HLbL) scattering, motivating a re-examination of HLbL modeling and inputs in the Standard-Model prediction of $(g-2)_\mu$, where hadronic effects dominate the theory uncertainty. Looking ahead, precision UPC measurements of $\gamma\gamma \to \pi^+\pi^-$ and $\gamma\gamma \to K^+K^-$ will be essential to test whether similar enhancements emerge for meson pairs, enabling a systematic map of any environment dependence across hadronic final states.

4 Summary

We report the direct observation of proton-antiproton pair production via photon-photon fusion in Au+Au UPCs at $\sqrt{s_{\rm NN}} = 200$ GeV. The $p\bar{p}$ invariant-mass spectrum is continuous over $2.05 < M_{p\bar{p}} < 2.4$ GeV/c^2, and the pair transverse-momentum distribution is sharply peaked below 0.1 GeV/c, both consistent with production by quasi-real photons. For $2.05 < M_{p\bar{p}} < 2.4$ GeV/c^2 and $p_T^{p\bar{p}} < 0.1$ GeV/c, the integrated cross section is measured to be $\sigma_{p\bar{p}} = 1.56 \pm 0.22\,(\text{stat.}) \pm 0.23\,(\text{syst.})$ μb. Photonuclear contributions are estimated to be negligible in this kinematic region, establishing $\gamma\gamma \to p\bar{p}$ as the dominant production mechanism. The quasi-real, ultra-strong electromagnetic fields in UPCs provide conditions close to the classical-field limit that underlies Schwinger-like vacuum excitation, and the present result extends such light-to-matter studies from elementary lepton pairs to baryon-antibaryon production.

Notably, the measured cross section exceeds expectations obtained by extrapolating from e^+e^- collider data, pointing to remaining theoretical uncertainties in relating different experimental environments and/or to additional dynamics relevant for composite hadrons. This tension motivates precision measurements of other $\gamma\gamma$-produced hadronic final states and further theoretical developments that consistently incorporate strong-field QED with non-perturbative QCD effects.

More broadly, the result offers an independent empirical constraint on $\gamma\gamma \to$ hadrons in a kinematic regime relevant to hadronic light-by-light scattering, a key ingredient in the Standard-Model prediction of $(g-2)_\mu$. It also establishes heavy-ion UPCs as a powerful laboratory for exploring photon-induced reactions and vacuum structure in extreme electromagnetic fields.

Acknowledgements

We thank the RHIC Operations Group and SDCC at BNL, the NERSC Center at LBNL, and the Open Science Grid consortium for providing resources and support. This work was supported in part by the Office of Nuclear Physics within the U.S. DOE Office of Science, the U.S. National Science Foundation, the Ministry of Science and Technology of China, National Natural Science Foundation of China, Chinese Academy of Science and the Chinese Ministry of Education, NSTC Taipei, the National Research Foundation of Korea, Czech Science Foundation and Ministry of Education, Youth and Sports of the Czech Republic, Hungarian National Research, Development and Innovation Office, New National Excellency Programme of the Hungarian Ministry of Human Capacities, Department of Atomic Energy and Department of Science and Technology of the Government of India, the National Science Centre and WUT ID-UB of Poland, German Bundesministerium für Bildung, Wissenschaft, Forschung and Technologie (BMBF), Helmholtz Association, Ministry of Education, Culture, Sports, Science, and Technology (MEXT), and Japan Society for the Promotion of Science (JSPS).

A Methods

This analysis is based on the STAR detector, which was designed with the purpose of searching for the Quark-Gluon Plasma. The STAR detector includes sub-detector systems such as Heavy Flavor Tracker (HFT), TPC, TOF, Barrel ElectroMagnetic Calorimeter (BEMC), Magnet, Muon Telescope Detector (MTD), Vertex Position Detector (VPD), BBC, ZDC, Endcap ElectroMagnetic Calorimeter (EEMC), among others [33] (Fig. 3).

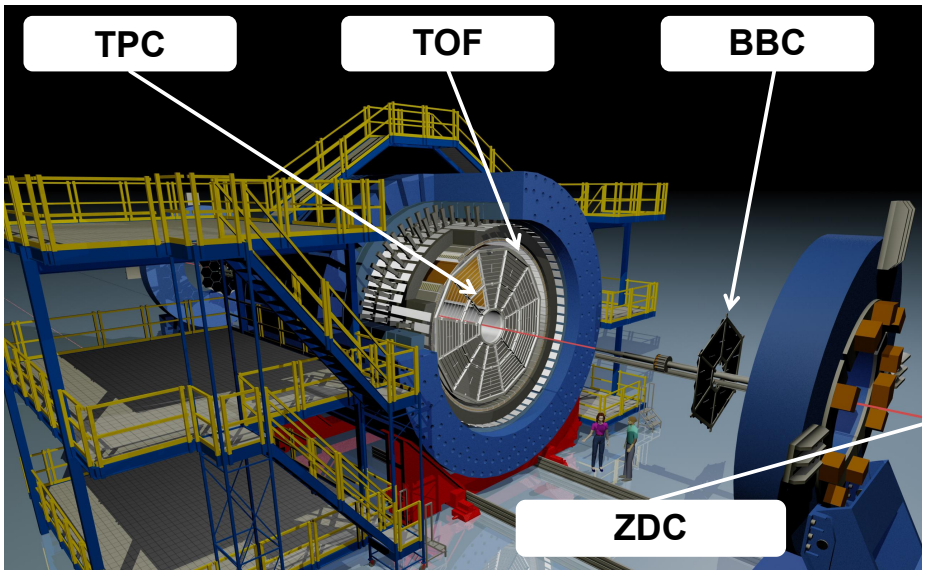

Figure 3: The schematic view of the STAR detector system.

In this analysis, TPC, TOF, BBC, and ZDC play important roles. The STAR TPC is a cylindrical detector with a length of 4.2 meters along the beam axis and a radial extent of 2 meters, operating within a 0.5 T solenoidal magnetic field. When charged particles traversing the gas volume, they ionize the gas, liberating electrons that drift toward the readout end-plates under an applied electric field. From the positions and arrival times of these electrons at the pixelated readout plane, the particle trajectory is reconstructed; its curvature $r_{\text{curvature}}$ yields the momentum via $p = 0.3 \times B \times r_{\text{curvature}}$.

The TOF detector encircles the TPC, spanning a range of $|\eta| < 0.9$ (η is the pseudorapidity of the single track, defined as $\eta = -\ln\left[\tan\left(\frac{\theta}{2}\right)\right]$, θ is the polar angle between the track and the beam direction), and full azimuthal coverage. The TOF detector employed the technology known as the Multi-gap Resistive Plate Chamber [76]. The TOF detector identifies particles by measuring the time they take to traverse a known distance, enabling the calculation of their mass. The BBC comprises a series of scintillator annuli positioned encircling the RHIC beam pipe at the eastern and western extremities of the STAR magnet's

poles. The ZDC system consists of two identical hadron calorimeters positioned symmetrically on the east and west sides of the STAR interaction region, each containing three longitudinal modules.

This analysis used data selected by the "UPC-Main trigger" collected in 2010 (Run10, 23 million events), 2011 (Run11, 18 million events) and 2014 (Run14, 102 million events) Au+Au collisions at $\sqrt{s_{\rm NN}} = 200$ GeV. Without loss of generality, we will use Run10 data as an example to introduce the analysis method in the following section.

A.1 Trigger Condition and Event Selection

The UPC-Main trigger is designed to accept events in which the impact parameter of two atomic nuclei is greater than the sum of the radii of the two nuclei, thereby resulting in no hadronic interaction processes occurring during the collision. The trigger conditions are listed below:

- Activity in the TOF (number of TOF hits between 2 and 6). UPC events typically contain only a small number of charged particles. The multiplicity information from TOF was utilized to assist in rejecting non-UPC events.
- No events in either East or West BBCs. Due to the typically low multiplicity of UPC events, if the BBCs were fired with an Analog-to-Digital Converter (ADC) sum > 20 (to prevent interference from noise signals), this usually indicates that a more traditional nuclear collision has occurred rather than a UPC event.
- Showers in both ZDCs. The electromagnetic fields induced by the fast-moving nucleus can also excite the other nucleus, causing it to emit neutrons. The ZDC-ADC are therefore required to select events with at least one neutron emitted on each side, i.e., the XnXn mode. The 0n mode (zero neutron emission) is not selected because it is indistinguishable from noise in the ZDC.
- The ZDC signal timing difference is constrained to be less than 511 Time-to-Digital Converter (TDC) channels. This condition is to ensure the interaction occurs within the acceptance of the TPC.

For each event selected by UPC-Main trigger, the reconstructed collision point, called the primary vertex, is required to be within ± 100 cm along the beam line from the detector center to reduce uncertainty from degraded TPC acceptance. For each event, we require exactly two tracks originating from the collision vertex with opposite charges and the global reference multiplicity (which is defined as the total number of charged particles within the full acceptance of the STAR detector) ≤ 4 to reject background events. For each single track, the p_T is required to be larger than 0.2 GeV/c and $|\eta|$ is required to be less than 0.9. The p_T range requirement is due to the fact that tracks with very low transverse momentum will undergo significant curvature in the magnetic field, causing them to spiral and fail to traverse the full length of the TPC. The $|\eta|$ range

requirement is necessary as the TOF efficiency diminishes significantly as $|\eta|$ approaches 1. Thus 0.9 was set as the selection criteria. To ensure high-quality track reconstruction, we require nHitsFit (the number of hit points in the TPC used for track fitting) ≥ 20 (Max nHitsFit = 46), nHitsDedx (the number of points used in the energy loss calculation) ≥ 15 (Max nHitsDedx = 32 for Run10 and Run11, Max nHitsDedx = 45 for Run14) and nHitsratio (the ratio of nHitsFit to the maximum possible numbr of TPC hits along the trajectory) ≥ 0.52. Typically, tracks with higher values of nHitsFit and nHitsDedx have a high quality momentum and dE/dx resolution. The nHitsRatio criterion helps to reject split tracks—if a track is incorrectly reconstructed as two separate tracks, this ratio typically falls below 0.5 for at least one of the tracks. Each track is required to match a TOF hit. This matching is achieved by projecting the track to the TOF barrel and requiring the projected position to fall within a predefined tolerance of a measured TOF hit.

A.2 Proton Pair Identification

Proton identification relies on the specific energy loss $\langle dE/dx \rangle$ measured by the TPC. The collected charge on the pixelated anodes-produced via avalanche amplification of the primary ionization electrons-is directly proportional to the energy loss rate of the original particle. To quantify this information, the deviation of a track's measured specific $\langle dE/dx \rangle$ from the expected value for a given particle species, normalized by the TPC's resolution, defines the $n\sigma$ variable used for particle identification. Figure 4 illustrates the $n\sigma_p$ distribution for single tracks after event selection, kinematic, and $n\sigma_e > 2$ requirements, where protons and anti-protons are distinctly separated from other particle species. This clear separation demonstrates the excellent particle identification capability of the TPC. Since we are interested in proton-antiproton pairs, a more useful quantity for identification is: $\chi^2_{p\bar{p}} = n\sigma_p^2 + n\sigma_{\bar{p}}^2$. Considering the potential overlap of electrons and pions within the $|n\sigma_p| < 2$ region at relatively high p_T (Fig. 5) and the p_T distribution of single track data (Fig. 6), the criteria of $n\sigma_e > 2$ and $n\sigma_\pi > 3$ are further required to ensure high proton purity.

In order to reject protons produced from collisions with the beam pipe and other materials ("knock out"), the distance-of-closest approach (DCA) between the proton and the primary vertex is required to be within 0.5 cm. This DCA requirement is not applied to antiprotons since there are no knock out antiprotons (Fig. 7).

A.3 Cosmic Ray Background

Although the aforementioned track selection criteria can filter out most of the background, there is a special type of background that can just pass through our selection criteria, which is the cosmic ray background. Primary cosmic rays are high-energy particle streams that originate from outer space and consist primarily of protons (90%), helium nuclei (9%) and other particles (1%). Upon entering the atmosphere, the primary cosmic rays interact with atomic nuclei

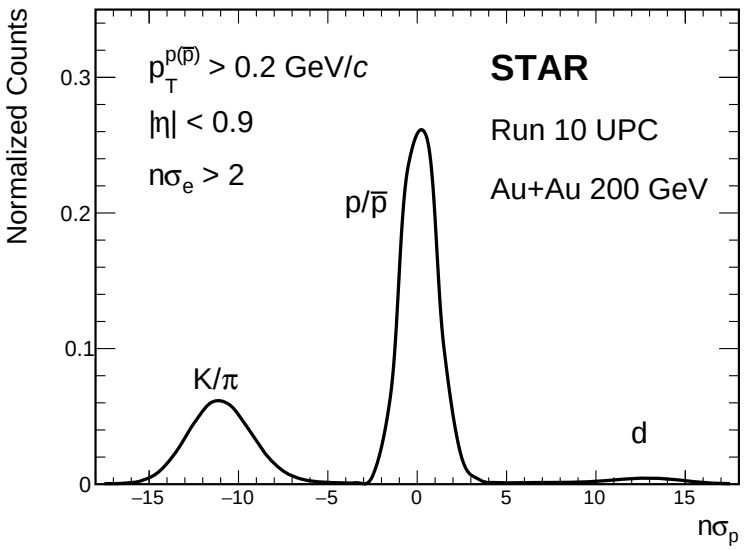

Figure 4: $n\sigma_p$ distribution for single tracks after selection. The clear separation of protons demonstrates the excellent PID capability of the TPC.

in the air molecules, resulting in an extensive air shower and producing an abundance of secondary particles. Although cosmic ray protons reaching the ground are few, they can still become our background. Cosmic ray protons can pass through the TPC and leave a track, but since the reconstruction of tracks in the TPC starts from the innermost layers and moves radially outward, the cosmic track will be reconstructed as two back-to-back opposite charge tracks due to the right-hand rule. These incorrectly reconstructed pairs of cosmic tracks pass all our selection criteria. Study of the cosmic-ray data collected by the STAR collaboration, under the trigger condition requiring hits in opposing top and bottom sectors of the TOF detector, shows that the $p\bar{p}$ pairs induced by such cosmic-ray protons are strongly localized near rapidity zero (Fig. 8). Therefore, we require a rapidity selection criteria $|Y^{p\bar{p}}| > 0.05$ to reject the cosmic ray background ($Y^{p\bar{p}} = \frac{1}{2}\ln\left(\frac{E^{p\bar{p}}+p_z^{p\bar{p}}}{E^{p\bar{p}}-p_z^{p\bar{p}}}\right)$, where $E^{p\bar{p}}$ and $p_z^{p\bar{p}}$ are the energy and the momentum along the beam direction of $p\bar{p}$ pair respectively).

A.4 Original Signal

After applying the above selection conditions, a total of 96 $p\bar{p}$ pairs were selected (left panel of Fig. 9). Due to the protons in the like-sign background primarily originating from knock-out, their distribution is quite different from that of antiprotons. Hence, it is appropriate to estimate the like-sign background using the geometric mean. The number of like-sign pairs $N_{like-sign}$ are calculated as

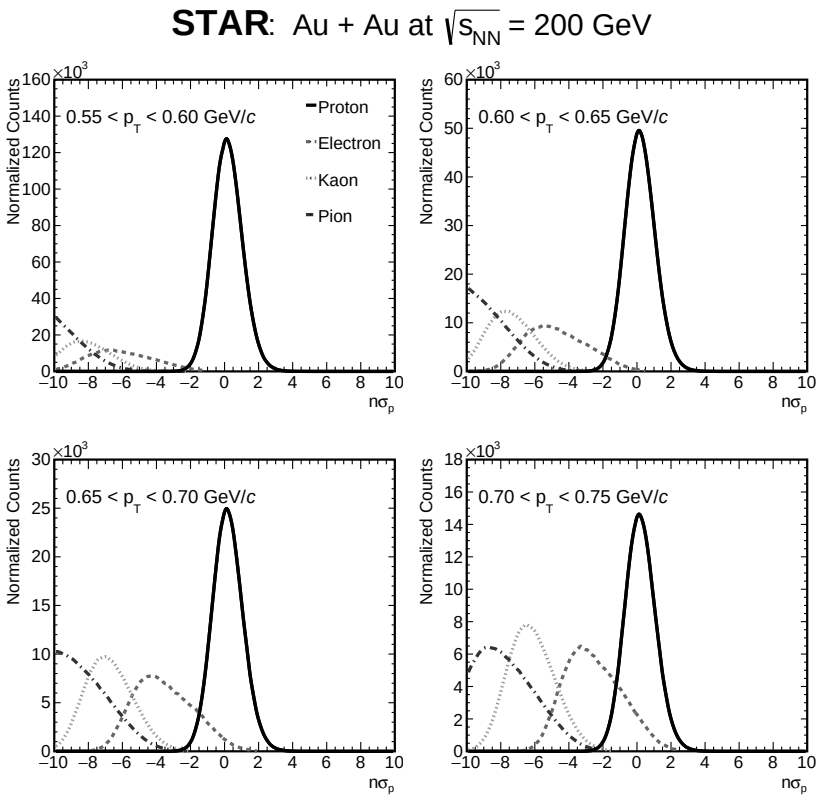

Figure 5: nσ_p distributions for different particles for different p_T range. Electron (dashed curve) and pion (dash-dotted curve) contamination increases with p_T.

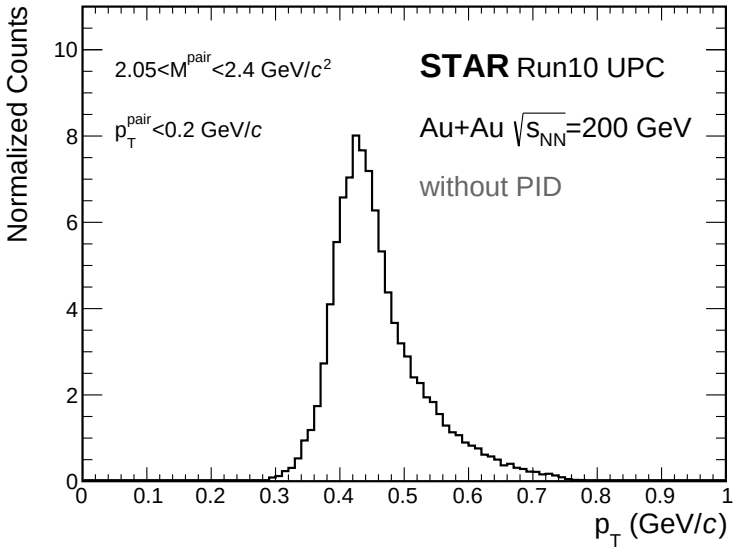

Figure 6: The p_T distribution of the single track before particle identification.

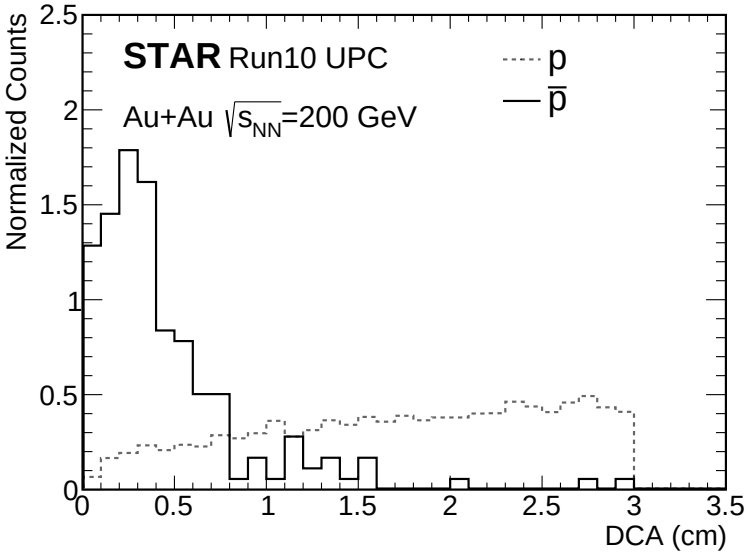

Figure 7: The DCA distribution for protons (dashed line) and antiprotons (solid line). The DCA distribution of protons is significantly larger than that of antiprotons due to protons knocked out from the detector materials.

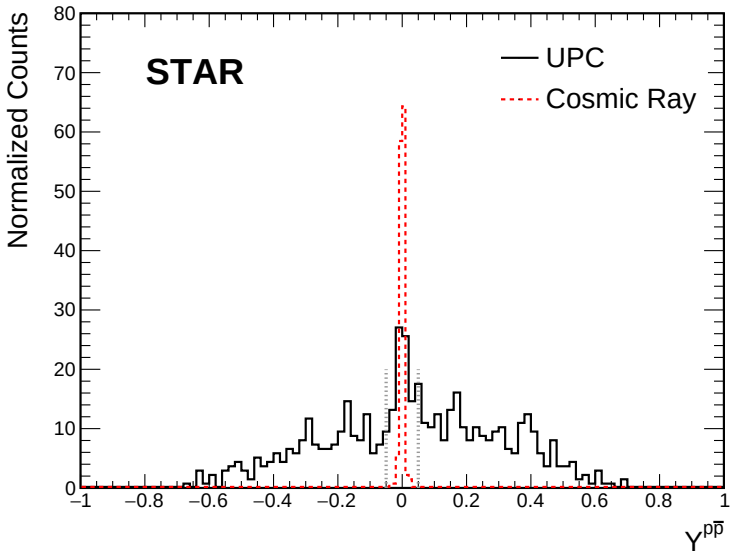

Figure 8: Pair rapidity distribution for UPC data (black solid line) and cosmic ray data (red dashed line). A sharp peak generated from cosmic ray is apparent at zero pair rapidity. Thus the selection criteria $Y^{p\bar{p}} > 0.05$ (gray dotted line) is required.

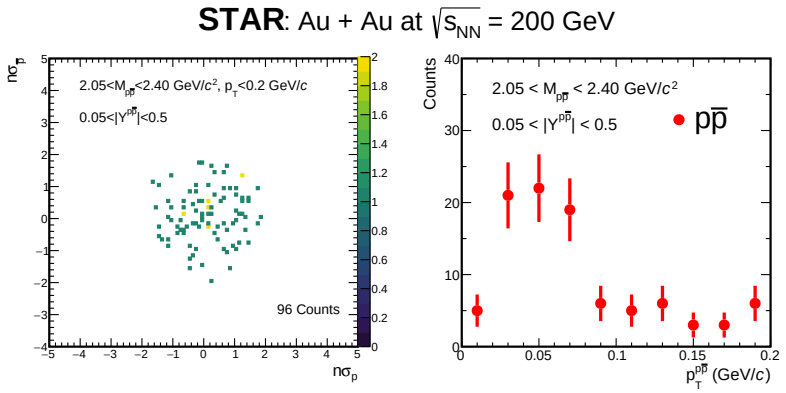

Figure 9: Left panel: The $n\sigma_p$ versus $n\sigma_{\bar{p}}$ distribution after applying all the selection conditions. Right panel: The p_T spectrum of the $p\bar{p}$ pairs, a significant peak is revealed in the region $p_T < 0.1\,\mathrm{GeV}/c$.

the geometry average of the N_{pp} and the $N_{\bar{p}\bar{p}}$:

$$N_{like-sign} = 2\sqrt{N_{pp} \times N_{\bar{p}\bar{p}}}. \tag{5}$$

The UPC process is free from hadronic interactions, thus no like-sign background was observed. The right panel of Fig. 9 shows the p_T distribution of the original signal. It can be observed that the original signal is primarily concentrated in the extremely low p_T region, which is consistent with the characteristics of photoproduction.

A.5 Purity Estimation

In principle, the $\chi^2_{p\bar{p}}$ for proton-antiproton pairs should be close to 0 and have an exponential distribution; the purity can be extracted by fitting the $\chi^2_{p\bar{p}}$ distribution. However, the current analysis lacks sufficient statistics to estimate the purity from the $\chi^2_{p\bar{p}}$ distribution. The pure proton/pion/electron samples from the Minimum Bias (MB) trigger were therefore used to estimate the purity of $p\bar{p}$ pair candidates. The proton and pion samples are selected using the mass information provided by TOF, while the electron sample is obtained by reconstructing electron-positron pairs and selecting the mass region of photon conversions ($M_{e^+e^-} < 0.012$ GeV/c^2). The purity of the proton is extracted with the following steps:

- Sampling the pair p_T, rapidity and invariant mass from the UPC data, use the two-body decay kinematics to sample the polar angle of the single proton in the proton-antiproton rest frame.
- Sampling the $n\sigma_p$, $n\sigma_e$ and $n\sigma_\pi$ with the given momentum of the proton and antiproton simultaneously from the pure proton sample. If the Monte-

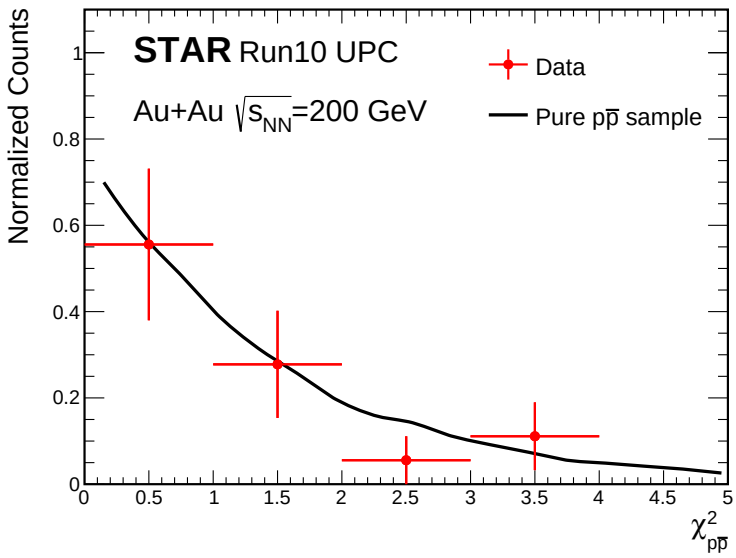

Figure 10: The $\chi^2_{p\bar{p}}$ distribution from MC sampling (black curve) and from UPC data (red points). The template can describe the data very well.

Carlo (MC) proton and antiproton both satisfy all our requirements, then calculate the $\chi^2_{p\bar{p}}$ of this MC pair. Such $\chi^2_{p\bar{p}}$ can be regarded as a template.

Fig. 10 shows the $\chi^2_{p\bar{p}}$ distribution from this MC sampling procedure and the UPC data. The MC (black curve) shape can describe the data (red points) very well. To further estimate how many electrons are mixed into our $p\bar{p}$ pairs, the same steps used for extracting the proton MC events are applied to the electron sample. Out of one million MC generated samples, no electron passed our PID requirement, which indicates that the purity of our $p\bar{p}$ pairs is larger than 99.9%.

A.6 Efficiency Correction

The efficiency corrections for this analysis can be categorized into three main categories: trigger, tracking, and proton identification. Trigger efficiency includes ZDC-ADC requirement efficiency, TOF multiplicity efficiency, and BBC veto efficiency. We use the ZDC-Monitor triggered data to extract the trigger efficiency. The ZDC-Monitor trigger contains only the same ZDC-ADC lower requirement condition and ZDC-TAC (Time to Amplitude Converter) condition as the UPC-Main trigger and no other trigger condition. The trigger efficiency except the ZDC-ADC lower requirement efficiency is extracted via a data-driven method. The ZDC-ADC lower requirement efficiency is extracted from fitting the ZDC-ADC distribution directly. For Run10, the total trigger efficiency is 35%.

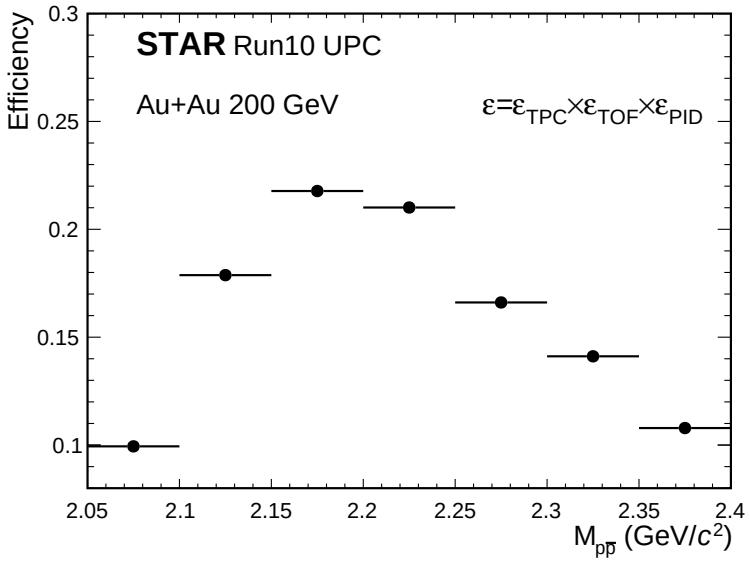

Figure 11: The efficiency versus the $p\bar{p}$ invariant mass, where the efficiency includes TPC efficiency, TOF efficiency, and PID efficiency.

The TPC efficiency is obtained with an embedding MC technique. The MC proton antiproton pairs are simulated using the GEANT package [77], taking into account the geometry and materials of the STAR detectors. The responses of the detectors and read-out electronics are also simulated, and the final simulated data are embedded into real data events. For each event, two MC tracks are simulated and processed through the same reconstruction procedures as real data. After that, the same track and topological requirements as for the real data are applied to the reconstructed MC proton-antiproton pairs. The final TPC efficiency is calculated as the ratio of the number of reconstructed MC $p\bar{p}$ pairs to the number of input MC $p\bar{p}$ pairs.

For TOF matching efficiency, we use the pure proton sample to extract the single proton TOF matching efficiency and calculate the pair efficiency via a MC method. For PID efficiency, a method similar to that used for estimating purity is employed to calculate the PID efficiency. The PID efficiency is calculated as the ratio of MC $p\bar{p}$ pairs within the acceptance that can pass the PID selection criteria ($\chi^2_{p\bar{p}} < 4$, $n\sigma_e > 2$ and $n\sigma_\pi > 3$) to the number of total MC $p\bar{p}$ pairs. The efficiency, comprising TPC, TOF, and PID efficiencies, is shown as a function of the $p\bar{p}$ invariant mass in Fig. 11. The rising-then-falling trend occurs because in the low-mass region, as the mass increases, the single-track p_T rises, leading to an increase in TPC and TOF efficiency, whereas in the high-mass region, the increase in single-track p_T causes PID efficiency to decrease (same mechanism as in Fig. 5).

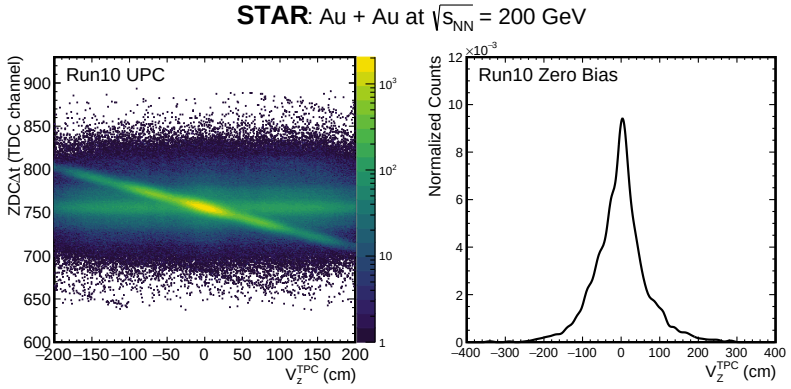

Figure 12: Left: Distribution of ZDCΔt versus V_z^{TPC}. A clear linear relationship can be seen. Right: The V_z distribution obtained via deconvolution method using zero-bias data.

A.7 Luminosity Correction

The luminosity measurement integrates beam collisions along the full length in the beam direction (z-axis), which extends beyond the acceptance of the TPC. The full Z-profile for the luminosity measurement is obtained from zero-bias data (events with no selection applied). The time difference (ZDCΔt) between the two ZDCs on opposite sides of the detector is used to determine V_z, the longitudinal position of the collision vertex, by measuring the relative times of particles along the collision axis. The relationship between the ZDCΔt and the V_z measured by TPC (V_z^{TPC}) is derived by fitting the ZDCΔt distribution with a Gaussian for each V_z^{TPC}, extracting the mean value of ZDCΔt ($\mu_{\Delta t}$) and its variance $\sigma_{\Delta t}$ (Fig. 12 left). The $\mu_{\Delta t}$ is expressed as $\mu_{\Delta t} = a * V_z^{TPC} + b$, where a and b are obtained from the fit. Then the ZDCΔt distribution can be written as the convolution of the distribution of $\mu_{\Delta t}$ with a Gaussian distribution:

$$f\left(\Delta t^{ZDC}\right) = \int_{-\infty}^{+\infty} f\left(\mu_{\Delta t}\right) g\left(ZDC\Delta t - \mu_{\Delta t}\right) d\mu_{\Delta t}. \tag{6}$$

The $f\left(\mu_{\Delta t}\right)$ can be obtained by deconvolution from Eq. 6, and the full V_z^{TPC} range can be estimated from the clear linearity relationship. Finally, the efficiency of $|V_z^{TPC}| < 100$ cm can be extracted from the full Z-profile (Fig. 12 right).

A.8 Systematic Uncertainties

The sources and the values of the systematic uncertainties are listed below:

- Luminosity: Common uncertainty for each run. The luminosity uncertainty from the Vernier scan technique arises from distinct experimental inputs: beam current measurements, relative beam position measurements and absolute beam position measurements (crossing angles) [78].

	Run10	Run11	Run14
Luminosity	10%	10%	10%
nHitsDedx	5%	3%	2%
nHitsFit	1%	1%	2%
DCA	1%	1%	1%
TOF	10%	9%	3%
PID	7%	7%	2%
V_z	1%	2%	2%
Total	17%	16%	12%

Table 1: Summary of the systematic uncertainties for each year.

- TPC efficiency: The uncertainty of the TPC efficiency is extracted from the difference of the nHitsDedx, nHitsFit and DCA distributions between the MC data and the UPC data.
- TOF efficiency: The uncertainty of the TOF efficiency is extracted from the difference between the TOF matching efficiency calculated using decay protons from $\Lambda \to p\pi^-$ satisfying $|n\sigma_p| < 1$ and that calculated using TPC-identified protons selected with a stricter requirement($|n\sigma_p| < 0.5$).
- PID efficiency: The uncertainty of the PID efficiency is extracted from the differences between the PID efficiency calculated from the data with different collision overlap regions (centrality).
- V_z requirement efficiency: The uncertainty of the V_z efficiency is extracted from the difference between the V_z efficiency calculated from UPC data and that from zero-bias data.

The uncertainties are listed in table 1. The total systematic uncertainty for each year is obtained by taking the square root of the sum of the squares of the individual uncertainties.

A.9 Cross Section Combination

Due to the varying detector efficiencies in different years, the data from each year have been efficiency-corrected separately. The cross section from different years are in good agreement with each other: the difference between Run10 and Run11 is 0.06 standard deviations, while the deviation of Run14 from Run10 and Run11 is 1.49 standard deviations. This discrepancy can be attributed to the lower efficiency and reduced raw signal of Run14, which result in a relatively larger statistical uncertainty. To further reduce the statistical uncertainties, we

combine the cross section from different years using the following formula:

$$mDen = \Sigma_i \frac{1}{\left(E^i_{stat}\right)^2}, \quad W_i = \frac{1}{\left(E^i_{stat}\right)^2 \times mDen} \tag{7}$$

$$\sigma_{combined} = \Sigma_i W_i \times \sigma_i, \quad E^{stat}_{combined} = \sqrt{\Sigma_i \left(W_i \cdot E^i_{stat}\right)^2}, \tag{8}$$

where i = Run10, Run11, and Run14, E^i_{stat} represent the statistical errors, $mDen$ is the sum of the weights, and W_i is the normalized weight for each individual year. Since the primary source of the uncertainty is the statistical uncertainty in this analysis, the systematic uncertainty is considered as entirely correlated for the three years:

$$E^{sys}_{combined} = \Sigma_i W_i \cdot E^i_{sys}, \tag{9}$$

where E^i_{sys} represent the systematic uncertainties for different years.

References

[1] P. A. M. Dirac. Quantum theory of emission and absorption of radiation. *Proc. Roy. Soc. Lond. A*, 114:243, 1927. doi: 10.1098/rspa.1927.0039.

[2] R. P. Feynman. Space-time approach to nonrelativistic quantum mechanics. *Rev. Mod. Phys.*, 20:367–387, 1948. doi: 10.1103/RevModPhys.20.367.

[3] J. S. Schwinger. Quantum electrodynamics. III: The electromagnetic properties of the electron: Radiative corrections to scattering. *Phys. Rev.*, 76: 790–817, 1949. doi: 10.1103/PhysRev.76.790.

[4] S. Tomonaga. On a relativistically invariant formulation of the quantum theory of wave fields. *Prog. Theor. Phys.*, 1:27–42, 1946. doi: 10.1143/PTP.1.27.

[5] S. L. Glashow. Partial Symmetries of Weak Interactions. *Nucl. Phys.*, 22: 579–588, 1961. doi: 10.1016/0029-5582(61)90469-2.

[6] S. L. Glashow, J. Iliopoulos, and L. Maiani. Weak Interactions with Lepton-Hadron Symmetry. *Phys. Rev. D*, 2:1285–1292, 1970. doi: 10.1103/PhysRevD.2.1285.

[7] D. J. Gross and F. Wilczek. Ultraviolet Behavior of Nonabelian Gauge Theories. *Phys. Rev. Lett.*, 30:1343–1346, 1973. doi: 10.1103/PhysRevLett.30.1343.

[8] H. D. Politzer. Reliable Perturbative Results for Strong Interactions? *Phys. Rev. Lett.*, 30:1346–1349, 1973. doi: 10.1103/PhysRevLett.30.1346.

[9] T. D. Lee and G. C. Wick. Vacuum Stability and Vacuum Excitation in a Spin 0 Field Theory. *Phys. Rev. D*, 9:2291–2316, 1974. doi: 10.1103/PhysRevD.9.2291.

[10] E. P. Tryon. Is the universe a vacuum fluctuation. *Nature*, 246:396, 1973. doi: 10.1038/246396a0.

[11] W. Heisenberg. Uber den anschaulichen Inhalt der quantentheoretischen Kinematik und Mechanik. *Z. Phys.*, 43:172–198, 1927. doi: 10.1007/BF01397280.

[12] J. Schwinger. Quantum electrodynamics. ii. vacuum polarization and self-energy. *Phys. Rev.*, 75:651–679, Feb 1949. doi: 10.1103/PhysRev.75.651.

[13] W. V. Houston and Y. M. Hsieh. The fine structure of the balmer lines. *Phys. Rev.*, 45:263–272, Feb 1934. doi: 10.1103/PhysRev.45.263.

[14] W. E. Lamb and R. C. Retherford. Fine Structure of the Hydrogen Atom by a Microwave Method. *Phys. Rev.*, 72:241–243, 1947. doi: 10.1103/PhysRev.72.241.

[15] H. A. Bethe. The Electromagnetic shift of energy levels. *Phys. Rev.*, 72: 339–341, 1947. doi: 10.1103/PhysRev.72.339.

[16] H. B. G. Casimir and D. Polder. The Influence of retardation on the London-van der Waals forces. *Phys. Rev.*, 73:360–372, 1948. doi: 10.1103/PhysRev.73.360.

[17] S. K. Lamoreaux. Demonstration of the Casimir force in the 0.6 to 6 micrometers range. *Phys. Rev. Lett.*, 78:5–8, 1997. doi: 10.1103/PhysRevLett.78.5. [Erratum: Phys.Rev.Lett. 81, 5475–5476 (1998)].

[18] J. S. Schwinger. On gauge invariance and vacuum polarization. *Phys. Rev.*, 82:664–679, 1951. doi: 10.1103/PhysRev.82.664.

[19] T. H. Maiman. Stimulated optical radiation in ruby. *Nature*, 187:493–494, 1960. doi: 10.1038/187493a0.

[20] D. Strickland and G. Mourou. Compression of amplified chirped optical pulses. *Optics Communications*, 56(3):219–221, 1985. doi: 10.1016/0030-4018(85)90120-8.

[21] K. A. Tanaka et al. Current status and highlights of the eli-np research program. *Matter and Radiation at Extremes*, 5:024402, 03 2020. doi: 10.1063/1.5093535.

[22] M. Harrison, Stephen G. Peggs, and T. Roser. The RHIC accelerator. *Ann. Rev. Nucl. Part. Sci.*, 52:425–469, 2002. doi: 10.1146/annurev.nucl.52.050102.090650.

[23] LHC Design Report Vol.1: The LHC Main Ring. 6 2004. doi: 10.5170/CERN-2004-003-V-1.

[24] V. M. Kaspi and A. Beloborodov. Magnetars. *Ann. Rev. Astron. Astrophys.*, 55:261–301, 2017. doi: 10.1146/annurev-astro-081915-023329.

[25] F. Krauss, M. Greiner, and G. Soff. Photon and gluon induced processes in relativistic heavy ion collisions. *Prog. Part. Nucl. Phys.*, 39:503–564, 1997. doi: 10.1016/S0146-6410(97)00049-5.

[26] C. A. Bertulani, S. R. Klein, and J. Nystrand. Physics of ultra-peripheral nuclear collisions. *Ann. Rev. Nucl. Part. Sci.*, 55:271–310, 2005. doi: 10.1146/annurev.nucl.55.090704.151526.

[27] J. Chen et al. Properties of the QCD matter: review of selected results from the relativistic heavy ion collider beam energy scan (RHIC BES) program. *Nucl. Sci. Tech.*, 35(12):214, 2024. doi: 10.1007/s41365-024-01591-2.

[28] E. Fermi. On the Theory of the impact between atoms and electrically charged particles. *Z. Phys.*, 29:315–327, 1924. doi: 10.1007/BF03184853.

[29] C. F. von Weizsäcker. Radiation emitted in collisions of very fast electrons. *Z. Phys.*, 88:612–625, 1934. doi: 10.1007/BF01333110.

[30] E. J. Williams. sowie eine im erscheinen begrifene fortsetzung dieser arbeit. *Proceedings of the Royal Society of London Series A*, 139:163, 1933. sowie eine im Erscheinen begrifene Fortsetzung dieser Arbeit.

[31] J. Luo et al. Probing the collision geometry via two-photon processes in heavy-ion collisions. *Nucl. Sci. Tech.*, 37(6):102, 2026. doi: 10.1007/s41365-026-01934-1.

[32] M. Harrison, T. Ludlam, and S. Ozaki. RHIC project overview. *Nucl. Instrum. Meth. A*, 499:235–244, 2003. doi: 10.1016/S0168-9002(02)01937-X.

[33] K. H. Ackermann et al. STAR detector overview. *Nucl. Instrum. Meth. A*, 499:624–632, 2003. doi: 10.1016/S0168-9002(02)01960-5.

[34] J. Adam et al. Measurement of e^+e^- Momentum and Angular Distributions from Linearly Polarized Photon Collisions. *Phys. Rev. Lett.*, 127(5):052302, 2021. doi: 10.1103/PhysRevLett.127.052302.

[35] G. Breit and J. A. Wheeler. Collision of two light quanta. *Phys. Rev.*, 46 (12):1087–1091, 1934. doi: 10.1103/PhysRev.46.1087.

[36] M. Aaboud et al. Evidence for light-by-light scattering in heavy-ion collisions with the ATLAS detector at the LHC. *Nature Phys.*, 13(9):852–858, 2017. doi: 10.1038/nphys4208.

[37] G. Aad et al. Observation of light-by-light scattering in ultraperipheral Pb+Pb collisions with the ATLAS detector. *Phys. Rev. Lett.*, 123(5):052001, 2019. doi: 10.1103/PhysRevLett.123.052001.

[38] S. Acharya et al. Photoproduction of K+K- Pairs in Ultraperipheral Collisions. *Phys. Rev. Lett.*, 132(22):222303, 2024. doi: 10.1103/PhysRevLett.132.222303.

[39] C. J. Biddick et al. A study of double tagged two photon reactions at spear. *Phys. Lett. B*, 97:320, 1980. doi: 10.1016/0370-2693(80)90610-3.

[40] M. Artuso et al. Measurement of cross-section for gamma gamma —> p anti-p. *Phys. Rev. D*, 50:5484–5490, 1994. doi: 10.1103/PhysRevD.50.5484.

[41] H. Hamasaki et al. Measurement of the proton - anti-proton pair production from two photon collisions at TRISTAN. *Phys. Lett. B*, 407:185–192, 1997. doi: 10.1016/S0370-2693(97)00728-4.

[42] G. Abbiendi et al. Measurement of the cross-section for the process $\gamma\gamma \to p\bar{p}$ at $\sqrt{s_{ee}} = 183 - 189$GeV at LEP. *Eur. Phys. J. C*, 28:45–54, 2003. doi: 10.1140/epjc/s2003-01171-y.

[43] P. Achard et al. $p\bar{p}$ pair production in two photon collisions at LEP. *Phys. Lett. B*, 571:11–20, 2003. doi: 10.1016/j.physletb.2003.05.005.

[44] C. C. Kuo et al. Measurement of gamma gamma —> p anti-p production at Belle. *Phys. Lett. B*, 621:41–55, 2005. doi: 10.1016/j.physletb.2005.06.036.

[45] X. Wu et al. Impact parameter manipulation in exclusive photoproduction in Electron-Ion Collisions. *Nucl. Sci. Tech.*, 36(9):157, 2025. doi: 10.1007/s41365-025-01704-5.

[46] X. Wu et al. Interference-induced entanglement in an effectively zero-lifetime particle pair. 2026. arXiv:2601.18503 [hep-ph].

[47] E. G. Judd et al. The evolution of the STAR Trigger System. *Nucl. Instrum. Meth. A*, 902:228–237, 2018. doi: 10.1016/j.nima.2018.03.070.

[48] J. Adams et al. Experimental and theoretical challenges in the search for the quark gluon plasma: The STAR Collaboration's critical assessment of the evidence from RHIC collisions. *Nucl. Phys. A*, 757:102–183, 2005. doi: 10.1016/j.nuclphysa.2005.03.085.

[49] C. Adler et al. The RHIC zero-degree calorimeters. *Nucl. Instrum. Meth. A*, 499:433–436, 2003. doi: 10.1016/j.nima.2003.08.112.

[50] C. A. Whitten. The beam-beam counter: A local polarimeter at STAR. *AIP Conf. Proc.*, 980(1):390–396, 2008. doi: 10.1063/1.2888113.

[51] W. J. Llope. The large-area time-of-flight upgrade for STAR. *Nucl. Instrum. Meth. B*, 241:306–310, 2005. doi: 10.1016/j.nimb.2005.07.089.

[52] M. Anderson et al. The Star time projection chamber: A Unique tool for studying high multiplicity events at RHIC. *Nucl. Instrum. Meth. A*, 499: 659–678, 2003. doi: 10.1016/S0168-9002(02)01964-2.

[53] M. Shao et al. Extensive particle identification with TPC and TOF at the STAR experiment. *Nucl. Instrum. Meth. A*, 558:419–429, 2006. doi: 10.1016/j.nima.2005.11.251.

[54] Y. Xu et al. Improving the dE/dx calibration of the STAR TPC for the high-pT hadron identification. *Nucl. Instrum. Meth. A*, 614:28–33, 2010. doi: 10.1016/j.nima.2009.12.011.

[55] J. Nystrand and S. Klein. Two photon physics in nucleus-nucleus collisions at RHIC. In *Workshop on Photon Interactions and the Photon Structure*, pages 263–277, 11 1998.

[56] T. H. Bauer, R. D. Spital, D. R. Yennie, and F. M. Pipkin. The Hadronic Properties of the Photon in High-Energy Interactions. *Rev. Mod. Phys.*, 50: 261, 1978. doi: 10.1103/RevModPhys.50.261. [Erratum: Rev.Mod.Phys. 51, 407 (1979)].

[57] C. Zhang, L. Zhang, and D. Shao. Photon induced proton and anti-proton pair production with ultraperipheral heavy ion collisions at RHIC. *Sci. China Phys. Mech. Astron.*, 68(12):121011, 2025. doi: 10.1007/s11433-025-2720-6.

[58] J.-Y. Hu, S. Lin, S. Pu, and Q. Wang. Light nuclei photoproduction in relativistic heavy ion ultraperipheral collisions. 2024. arXiv:2407.06091 [hep-ph].

[59] S. Afanasiev et al. Photoproduction of J/psi and of high mass e+e- in ultra-peripheral Au+Au collisions at s**(1/2) = 200-GeV. *Phys. Lett. B*, 679:321–329, 2009. doi: 10.1016/j.physletb.2009.07.061.

[60] J. Adam et al. Measurement of an excess in the yield of J/ψ at very low p_{T} in Pb-Pb collisions at $\sqrt{s_{\mathrm{NN}}} = 2.76$ TeV. *Phys. Rev. Lett.*, 116(22):222301, 2016. doi: 10.1103/PhysRevLett.116.222301.

[61] J. Adam et al. Observation of excess J/ψ yield at very low transverse momenta in Au+Au collisions at $\sqrt{s_{\mathrm{NN}}} = 200$ GeV and U+U collisions at $\sqrt{s_{\mathrm{NN}}} = 193$ GeV. *Phys. Rev. Lett.*, 123(13):132302, 2019. doi: 10.1103/PhysRevLett.123.132302.

[62] C. Mayer. Coherent photo-production of ρ^0 mesons in ultra-peripheral Pb-Pb collisions at the LHC measured by ALICE. *EPJ Web Conf.*, 81: 02011, 2014. doi: 10.1051/epjconf/20148102011.

[63] L. Adamczyk et al. Coherent diffractive photoproduction of ρ^0mesons on gold nuclei at 200 GeV/nucleon-pair at the Relativistic Heavy Ion Collider. *Phys. Rev. C*, 96(5):054904, 2017. doi: 10.1103/PhysRevC.96.054904.

[64] W. Zha et al. Coherent J/ψ photoproduction in hadronic heavy-ion collisions. *Phys. Rev. C*, 97(4):044910, 2018. doi: 10.1103/PhysRevC.97.044910.

[65] W. Zha et al. Double-slit experiment at fermi scale: coherent photoproduction in heavy-ion collisions. *Phys. Rev. C*, 99(6):061901, 2019. doi: 10.1103/PhysRevC.99.061901.

[66] J. R. Forshaw, R. Sandapen, and G. Shaw. Color dipoles and rho, phi electroproduction. *Phys. Rev. D*, 69:094013, 2004. doi: 10.1103/PhysRevD.69.094013.

[67] S. Navas et al. Review of particle physics. *Phys. Rev. D*, 110(3):030001, 2024. doi: 10.1103/PhysRevD.110.030001.

[68] M. L. Miller, K. Reygers, S. J. Sanders, and P. Steinberg. Glauber modeling in high energy nuclear collisions. *Ann. Rev. Nucl. Part. Sci.*, 57:205–243, 2007. doi: 10.1146/annurev.nucl.57.090506.123020.

[69] S. D. Drell. Production of Particle Beams at Very High Energies. *Phys. Rev. Lett.*, 5:278–281, 1960. doi: 10.1103/PhysRevLett.5.278.

[70] P. Soding. On the Apparent shift of the rho meson mass in photoproduction. *Phys. Lett.*, 19:702–704, 1966. doi: 10.1016/0031-9163(66)90451-3.

[71] F. Afzal et al. Baryon anti-Baryon Photoproduction Cross Sections off the Proton. 2025. arXiv:2510.26890 [nucl-ex].

[72] L. Wang, X. Li, Z. Tang, X. Wu, and W. Zha. Calculations of di-hadron production via two-photon processes in relativistic heavy-ion collisions. *J. Phys. G*, 53(3):035102, 2026. doi: 10.1088/1361-6471/ae491c.

[73] S. R. Klein et al. STARlight: A Monte Carlo simulation program for ultra-peripheral collisions of relativistic ions. *Comput. Phys. Commun.*, 212: 258–268, 2017. doi: 10.1016/j.cpc.2016.10.016.

[74] W. Zha et al. Initial transverse-momentum broadening of Breit-Wheeler process in relativistic heavy-ion collisions. *Phys. Lett. B*, 800:135089, 2020. doi: 10.1016/j.physletb.2019.135089.

[75] D. Millers and J. F. Gunion. Q^2 Dependence of Exclusive Baryon - Anti-baryon Production in Photon-photon Collisions. *Phys. Rev. D*, 34:2657, 1986. doi: 10.1103/PhysRevD.34.2657.

[76] W. J. Llope. Multigap RPCs in the STAR experiment at RHIC. *Nucl. Instrum. Meth. A*, 661:S110–S113, 2012. doi: 10.1016/j.nima.2010.07.086.

[77] S. Agostinelli et al. GEANT4 - A Simulation Toolkit. *Nucl. Instrum. Meth. A*, 506:250–303, 2003. doi: 10.1016/S0168-9002(03)01368-8.

[78] A. Marotta and K. Drees. ZDC effective cross section for Gold-Gold Collisions During RHIC'S Run 16. *JACoW*, IPAC2024:MOPC02, 2024. doi: 10.18429/JACoW-IPAC2024-MOPC02.